Autonomous millimeter scale high throughput battery research system (Auto-MISCHBARES)

Fuzhan Rahmanian[1,2,4,5,6*], **Stefan Fuchs**[1,2], **Bojing Zhang**[1,2,4,5,6], **Maximilian Fichtner**[1,3], **and Helge Sören Stein**[1,2,4,5,6*]

[1]Helmholtz Institute Ulm, Applied Electrochemistry, Helmholtzstr. 11, 89081 Ulm, Germany
[2]Karlsruhe Institute of Technology, Institute of Physical Chemistry, Fritz-Haber-Weg 2, 76131 Karlsruhe, Germany
[3]Karlsruhe Institute of Technology, Institute of Nanotechnology, , 76021 Karlsruhe, Germany
[4]Present address: Technische Universität München, School of Natural Sciences, Department of Chemistry Lichtenbergstr 4, 85748 Garching, Germany
[5]Present address: Technische Universität München, Munich Data Science Institute, Walther-von-Dyck-Straße 10, 4, 85748 Garching, Germany
[6]Present address: Technische Universität München, Munich Institute for Robotic and Machine Intelligence, Georg-Brauchle-Ring 60-62, 80992 Munich, Germany
[*]corresponding author(s): Helge Sören Stein (helge.stein@tum.de),
Fuzhan Rahmanian (fuzhan.rahmanian@tum.de)

ABSTRACT

Discoveries of novel electrolyte-electrode combinations require comprehensive structure-property-interface correlations. Herein, we present an autonomous millimeter scale high-throughput battery research system (MISCHBARES) operated by hierarchical autonomous laboratory automation and orchestration (HELAO) which integrates modular research instrumentation and AI control. This paper will present cathode electrolyte interphase (CEI) formation in lithium-ion batteries at various potentials by correlating high-throughput electrochemistry and spectroscopy. We believe quality control and complex data analysis to be the missing puzzle piece towards more complex workflow automation. Auto-MISCHBARES integrates automatic quality control for both hardware and software to ensure high reliability through an on-the-fly fidelity assessment of each individual experiment. Data analysis is achieved through our Modular and Autonomous Data Analysis Platform (MADAP) in our presented platform, which is capable of performing a fully automated analysis of various voltammetry measurements in real-time. Integration of MISCHBARES and MADAP through HELAO enables versatile and complex active learning workflows in the discovery of new materials. We demonstrate this integrated workflow for reliable charging/discharging protocols.

1 Introduction

Automated quality control and data interpretation are the missing puzzle pieces towards prolonged walk-away-times in closed loop experimentation[1]. Early demonstrations of closed loop experiments included mostly error resilient measurement and facile data analysis, but the step towards complex and interrelated experimentation necessitates more robust data quality assessment. The evolution of these automated experiments towards truly autonomous Material Acceleration Platforms (MAPs) require integration of experimental processes, data management, and strategic decision-making[2]self-driving laboratories (SDLs)[3,4]. Laboratories such as BEAR[5], ARES[6], Clio[7], equipped with advanced frameworks are instrumental in boosting operational efficiency and research safety[8]. These technological leaps not only streamline experimental processes, but also enable scientists to undertake deeper and more intricate inquiries, accelerating discovery in various scientific domains[9,10]. Additionally, the integration of AI and machine learning (ML) allows for efficient exploration of complex chemical and material terrains[10,11]. SDLs, in particular, show the potential to accelerate research output by up to 30 times[9]. By automating and digitalizing processes, these systems increase experimental accuracy and walk away time[4].

1.1 The challenge of multifidelity and scability

There is a sprawl of MAPs in various fields[12–14] but unique challenges abound to non-aqueous battery research have resulted in but a few larger MAP efforts[15,16]. This complexity arises from the special housing and safety measures necessary to conduct battery research and a large chemical space for optimizing e.g. electrolytes, electrodes, design, and physical properties[17–19]. Significant efforts have been made in each of these areas, in particular, in electrolyte optimization; for instance, Dave et al.[20] developed an autonomous workflow which was able to combine 251 aqueous electrolyte salts for a mixed-anion sodium electrolyte. This workflow analyzed the ionic conductivity and electrochemical stability in approximately 25 minutes. In

subsequent work, they extended their study in a non-aqueous system[7] and optimized the electrolyte formulation for a single salt and ternary solvent design at various ratios for Lithium-ion batteries (LiBs) by utilizing a robotic platform. However, the autonomous investigation on CEI and solid electrolyte interphase (SEI) within MAPs are not extensively explored[21–23]. This highlights the ongoing need for innovative approaches in battery research, especially in understanding and optimizing the complex interactions at these interfaces[24,25]. A primary challenge in developing a system capable of providing a multifaceted solution for the next generation of battery materials[19] is the substantial costs involved in integrating a single laboratory with all the necessary devices[26]. However, this integration is essential as conducting comprehensive tests, such as correlating electrochemical and spectroscopic tests, is crucial for achieving multifidelity. Additionally, due to variations arising from different samples, this correlation and integration within a single lab on a single sample become even more important. This approach ensures consistency and reliability of results, as it effectively minimizes discrepancies that might occur from diverse laboratory environments.

1.2 The challenge of Designing an integrative Database solution

To address the challenges of multi-device testing on a single sample, the development of a robust data management is essential[25,27–29]. This system must enable seamless integration and communication across various instruments and bridge physical and temporal gaps in experimental stages that often exist between disparate experimental phases[30,31]. Such advancements are crucial in SDLs, where progress has been hindered by a lack of a standardized and user-friendly software with intuitive operational guidelines[15]. Efficient data management and experimental planning enables rapid processing and interpretation of high dimensional data, which unravel physio-chemical relations that surpass the analytical capacity of conventional approaches[1,32,33]. It also facilitates the incorporation of AI agents and Deep Learning (DL) tools, which can further accelerate exploration in chemical spaces and reduce recourse allocation[33–35]. This approach is in line with significant scientific efforts, as demonstrated by Pascazio et al.[36] in chemistry and in other domain[10], which emphasize the importance of consistent data quality protocols and data acquisition methods, in compliance with FAIR data principles[37].

1.3 Reliable cognitive computing approaches

In autonomous experimental setups, replicating burdensome human-intensive tasks, such as material sufficiency management or equipment cleaning, is challenging[2,38]. Simultaneously, these ensure the reliability and fidelity of measurements and require rigorous validation for experimental accuracy and consideration of potential hardware and software flaws[39]. The integration of ML and computer vision methods, as proposed in recent studies[4,40,41], can significantly improve system robustness and is crucial to monitor parameter validity in real time[4]. The goal is to achieve data integrity and support AI planners in informed decision-making. This is particular beneficial for non-aqueous battery systems experimentation in gloveboxes, where assembling and controlling multiple experiments present complexities that even with human intervention may prove challenging to manage effectively. These developments, thus, signify a transformative shift in scientific experimentation towards enhanced precision and reliability[40], highlighted by the critical need to recognize and address the technical challenges in experiment-specific boundaries to ensure results are both comprehensible and reproducible[14,42].

To advance the MAPs and overcome existing constrains[9,10], we introduce the AUTO-MISCHBARES, a reliable open-source framework designed for fully unsupervised operations. Building upon our earlier work in multithreaded asynchronous web-based frameworks[31], it integrates real-time analysis and feedback, thus enhancing experimental processes. This platform, features automated capabilities for a range of electrochemical measurements, as showcased in our study of the CEI on battery electrodes. We conducted sequential measurements by utilizing an open-cell setup[43] and characterized them using near-ambient pressure X-ray photoelectron spectroscopy (XPS). The agnostic nature of our framework ensures its adaptability for diverse organic and inorganic materials. This platform not only can accelerate research but also facilitates the sharing of validated data, helping scientist in the efficient extraction and transfer of information within the community[38,44].

2 Results and discussions

2.1 Framework overview

Material acceleration platforms can be developed by integrating four key elements from multiple hubs; The DeviceHub consists of hardware components responsible for moving and measuring. ServerHub ensures robust operations and communication workflow through orchestration and API design; The DataHub manages the database environment, and is a key for data integrity and accessibility; Lastly, the MultiAnalysisHub provides a wide spectrum of analytics, from statistical assessments to computer vision methods[47]. The integration of all the Hubs is the precursor of acceleration in material development[15,48] and therefore, by following this design philosophy, our Auto-MISCHBARES platform is developed to perform fully autonomous electrochemical measurements and is tailored to study the formation of SEI and CEI. In addition, it can monitor oxidation state changes in active materials.

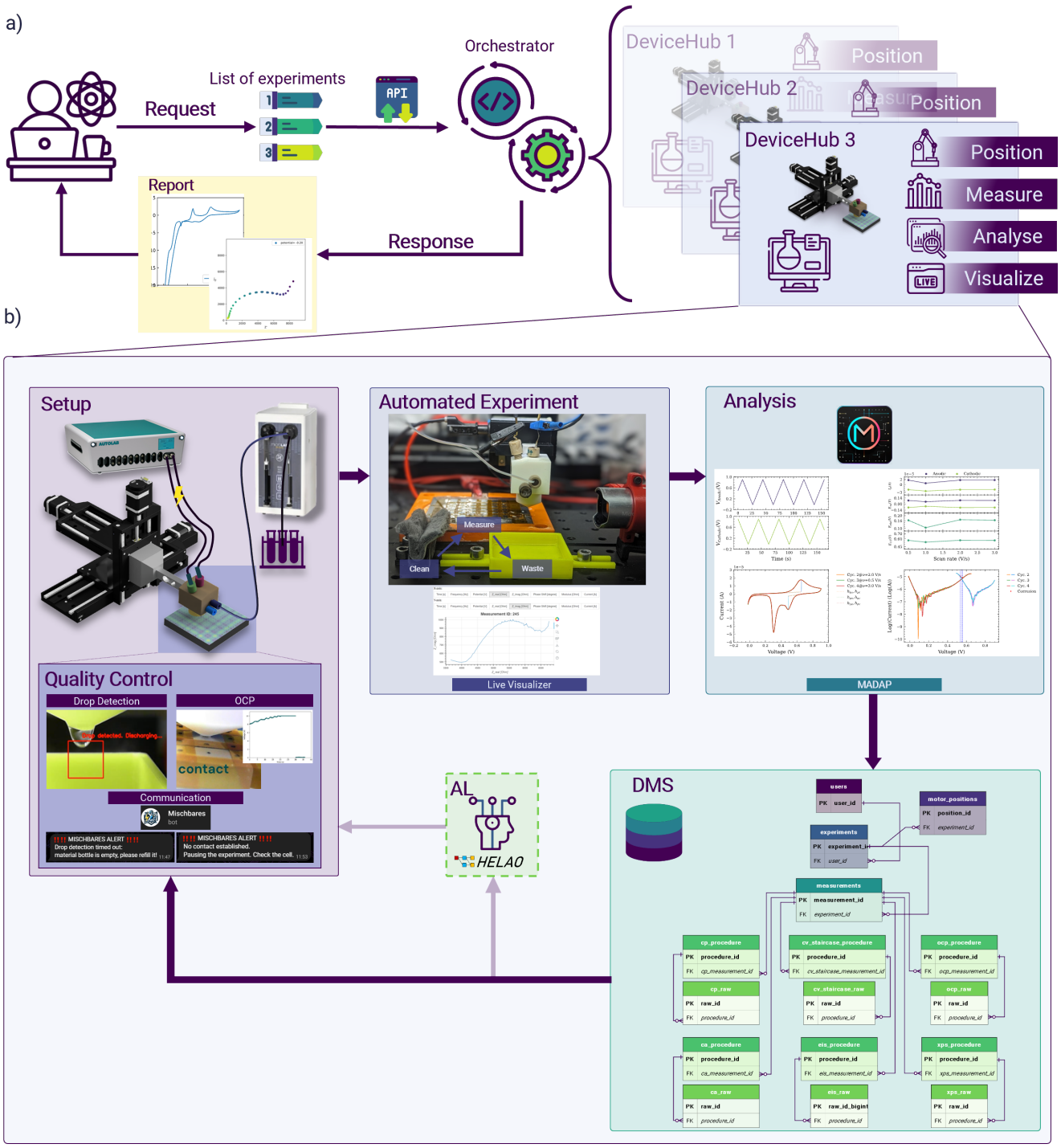

Figure 1. Schematic representation of the experimental management system of Auto-MISCHBARES[45]. The interface (Supp. 1) allows researchers to formulate a series of experimental electrochemical protocols, which are then dispatched to a central orchestrator via an Application Programming Interface (API). The orchestrator, serving as a control system, manages the scheduling, execution, and monitoring of the experimental array by delivering actions to the individual Hubs, which are the granular unit of activity and can execute actions tasks such as positioning, measurement, real-time analytical processing and provides the basis for live visualization. Upon the completion of individual experiments or a sequence thereof, the orchestrator compiles and dispatches a comprehensive analytical report to the experimentalist. The DeviceHub features a high-precision robotic manipulator adept at positioning the Scanning Droplet Cell (SDC) head accurately onto the substrate, where a Hamilton Microlab 600 precision syringe system [c] delivers electrolyte directly when contact is established. The Autolab Potentiostat [b] is employed to perform electrochemical measurements once the system is primed for analysis. Quality control protocols, including drop and contact detection and chatbot-based communication, facilitate automation and oversight of the experimental processes. Furthermore, experiments proceed in three automated stages: waste disposal, cleaning, and electrochemical measurement, each executed according to predefined specifications and with real-time plotting provided by a Bokeh[46] visualizer for immediate "at-a-glance" feedback. Post-measurement, the data undergoes immediate analysis via MADAP, which calculates electrochemical markers and generates corresponding plots for in-depth analysis. This processed data is then systematically cataloged in a Data Management System (DMS), ensuring data provenance, facile retrieval, and compartmentalization in alignment with the Findable, Accessible, Interoperable, and Reusable (FAIR) principles. It is possible to optimize the subsequent experiment with active learning (AL) algorithms through the HELAO platform.

2.1.1 ServerHub

This platform represents an advanced extension of our initial ServerHub, HELAO[31]. It is capable of executing experiments both sequentially and in parallel, and allows for the integration of an active learning decision-maker to orchestrate tasks across instruments. The complete workflow is illustrated in Figure 1a. At the beginning, researchers configure experimental setups and schedule multiple, dynamic batches of experiments through a user-friendly and modular interface (Supp. 1). The user interface (UI) is constructed using HTML, and CSS with dynamic functionalities implemented in Node.js and facilitates easy browsing with a diverse array of electrochemical protocols. This interaction layer is further enhanced by Flask[49], a Python-based web framework, to streamline user engagement. Once single or multiple experimental batches are designed, the configurations are passed to the Python back-end, requiring no additional user intervention, and are translated to FastAPI requests. The central orchestrator will then efficiently schedule and manage high-throughput experimentation in an asynchronous manner. After the execution of all requested experimental batches, the operator receives a response from the orchestrator with a comprehensive report detailing all experimental steps, their timestamps, and outcomes.

2.1.2 DeviceHub

In this study, we define our DeviceHub as an open cell, miniaturized 3-electrode-cell setup. known as the SDC[43]. This setup consists of a gold reference electrode (RE) and a platinum counter electrode (CE), both positioned within a movable cell housing made from polytetrafluoroethylene (PTFE). This housing utilizes electrode spots on a planar substrate functioning as the working electrode (WE). The electrochemical system is connected to a stepper motor [a] and a multichannel potentiostat device [b]. Additionally, a syringe pump system [c] is connected via an inlet to the cell. This configuration allows for precise delivery of the desired electrolyte formulation, as well as enabling accurate positioning over the targeted measurement area on the WE substrate and the deposition of a single droplet of electrolyte. Upon contact of all three electrodes, the system is ready to execute the selected protocols (Fig. 1b, Section Setup).

2.1.3 MultiAnalyseHub

A key challenge is maintaining the reliability of results, crucial for managing potential risks since a plethora of variables and parameters are prone to errors during experimentation[2]. These include tasks typically simple for humans, such as removal of salt accumulation, replenishing depleted electrolyte bottles, ensuring electrical connection at the hardware level, and maintaining safe thresholds for measurement parameters at the software level. Failure to address these aspects could not only lead to experimental inaccuracies but also in substantial time and resource wastage. The integration of mitigation strategies is a key step towards realizing a truly autonomous laboratory[48]. Thus, we enhance our platform by implementing mechanisms for providing critical feedback and real-time analysis throughout the experimental stages (Fig. 1b, Section Quality Control). This informs researchers of ongoing progress and potential failures, and enhance trustworthiness of high-throughput experimentation.

The initial quality control (QC) assessment in our system is monitoring material sufficiency at the electrolyte exchange stage for each measurement. A key component of this process is the Droplet Detection routine, designed to verify proper flushing. This detection is implemented using OpenCV library[50] for computer vision tasks and analyzes a video streams to detect the presence of a drop[51]. The algorithm selects a specific region of interest (ROI) in the video frame, converts this segment into grayscale and applies a Gaussian blur to minimize noise. By continuously calculating the absolute difference between the initial frame and subsequent frames within the ROI, the system can detect motion. A non-zero sum in the thresholded image within this area is indicative of a drop's presence. In addition, visual feedback is provided on the monitor for user verification and oversight.

Once the electrolyte has been exchanged, there is a chance of residual material remaining attached to the head of the SDC, which can lead to salt formation, crystallization, or inconsistencies in later measurements. We expand our control protocol and incorporate a mandatory movement of the SDC head to a wiping pad, ensuring the removal of any leftover electrolyte. Following this preparation, the stepper motor positions the SDC head over the designated measurement area of the WE.

Additional QC is implemented to precisely control the movement of the SDC head and ensure optimal electrical connectivity with the substrate in the coming measurement. This mechanism is designed to gradually lower the SDC head, performing the descent in small, constant steps. This approach secures each movement to stay within a defined threshold to prevent excessive force on the head. For stepwise monitoring of electrical potential, frequent control measurements are integrated with potentiostatic endpoints of the ServerHub. The data is then used to determine successful contact with the substrate, indicated by a sharp decay in potential towards zero. If contact is not established within the initial steps, the routine initiates corrective measures. These include the controlled addition of electrolyte and periodic potential measurements, along with emergency procedures in place for unresolved non-contact situations. Upon measurement initiation, an established threshold for experimental procedures prevent overshooting, thus ensuring safety. Throughout the entire QC process, continuous feedback is

[a] https://www.owis.eu/en/
[b] https://www.metrohm.com/de_de/products/a/ut30/aut302n_s.html
[c] https://www.hamiltoncompany.com/laboratory-products/microlab-600/syringe-pump

provided with logging and the option of communication through a Telegram chatbot, which informs the experimentalist at checkpoints and about potential failures, especially beneficial of unsupervised experimentation.

Our modular and versatile data analysis framework, MADAP[52], capable of analyzing a variety of electrochemical protocols, is integrated into our high-throughput automated workflow. It enables the real-time transformation of raw measurement into analyzed results for each experiment. The strength of this framework lies in its ability to simultaneously plot the raw and processed data (Fig. 1b, Section Analysis). It also generates reports and summaries in compliance with FAIR principles, with protocols formatted JSON and CSV files for individual experiments. MADAP capabilities offer a rapid assessment of experimental quality and can yield valuable scientific insights[3,47].

2.1.4 DataHub

The provenance of data is central in drawing conclusions from raw data[30,53,54]. This necessitates active tracking of acquisition and processing. To address the challenge of managing these complexities, our DMS implements a real-time approach in the context of the DataHub which is backed by our local PostgreSQL Database, designed to dynamically handle meta, raw, and analyzed data. It consists of several interconnected tables that capture specific details of the experiments. The `experiments` table forms the core of the database, stores essential metadata, such as material, date, and operator information (Fig. 1b, Section DMS). This is complemented by the `users` table, which details the researchers involved, ensuring traceability and accountability. The `motor_positions` table logs the specific operational data such as precise motor positions for the SDC head, adding further detail to the experimental records. Each type of electrochemical measurement in the database features paired procedure and raw tables. The `procedure` tables encapsulate the unique parameters and settings of every measurement, while the `raw` tables record granular empirical data. Key metrics, provided by MADAP and passed to HELAO, support the facilitation of ML algorithm usage when handling large data volumes through web server communication. Robust data integrity is ensured through primary and foreign keys, enabling complex queries that link procedures raw data, and experimental metadata. Additionally, the database incorporates sequences for auto-generating Unique Identifiers (UIDs), streamlining data entry and retrieval. This cohesive database system adheres to FAIR principles[37], to establish the integrity of experimental data while enhancing its accessibility, usability and interpretability[55]. This infrastructure minimizes human error in automated settings and is engineered to facilitate the correlation of electrochemical and spectroscopic tests, offering a unified platform for comprehensive multi-modal data analysis.

The integration of the four key hubs defines our robust Auto-MISCHBARES platform[45,51], streamlining sequential experimentation through unified process control, scheduling, feedback, and advanced real-time data management, encompassing measurement, validation, and analysis. Its modular design and multiple unit-tests ensure ease of expansion and adaptability for users.

2.2 Experimental procedure

Our platform is designed for investigating the formation of the CEI, which is influenced significantly by the type of active material, the inactive components of the composite electrode, and the electrolyte formulation[56,57]. Crucially, it eliminates the need for cell disassembly for ex-situ measurements, thus minimizing the risk of mechanical alterations. To demonstrate the reliability and reproducibility of our proposed framework, we investigate the evolution of CEI in lithium iron phosphate (LFP), a well-studied cathode material used in commercial batteries[58–60]. We used 1 M $LiPF_6$ solution in a mixture of ethylene carbonate (EC):ethyl methyl carbonate (EMC) in a 3 : 7 weight ratio as the electrolyte (E-lyte, Germany). The entire setup was maintained in a nitrogen-filled glovebox. It is important to note that electrolyte evaporation can occur due to the open-cell-setup. This poses challenges for long-term cycling tests, however, it offers distinct advantages for a variety of short-term measurements, which would otherwise require extensive assembly, disassembly, and electrode post-treatment. We designed our high-throughput sequential experimentation protocol using cyclic voltammetry (CV) tests, which are stopped at different potentials during the second cycle to analyze features related to redox reactions, and repeated the procedure two times. Our novel approach to cathode electrode preparation involved screen-printing onto the substrate. This method minimizes material usage and precisely defines the active material area. For each experiment, the SDC head is positioned at the predefined measurement spot, where it dispenses a droplet of electrolyte, and ensures electrical connection before performing CV. Upon completing a series of experiments, it is necessary to remove the excess $LiPF_6$ salt residue, a byproduct of electrolyte evaporation, from the electrodes. This is achieved by depositing a droplet of propylene carbonate (PC) on each measurement spot, allowing it to soak for three minutes to dissolve the salt, and then aspirating it using the SDC head. This cleaning process is repeated three times. Once the cleaned sampled are dried, they are transferred for ex-situ XPS analysis to characterize the synthesized CEI at different potentials and identify the formation stages of its components.

2.2.1 Reproducibility towards electrode fabrication

In our setup, electrodes were fabricated through screen-printing to ensure reproducible dimensions and alignment on a predefined grid. This method effectively decouples the electrodes from the electrolyte spreading area, thereby minimizing cross-

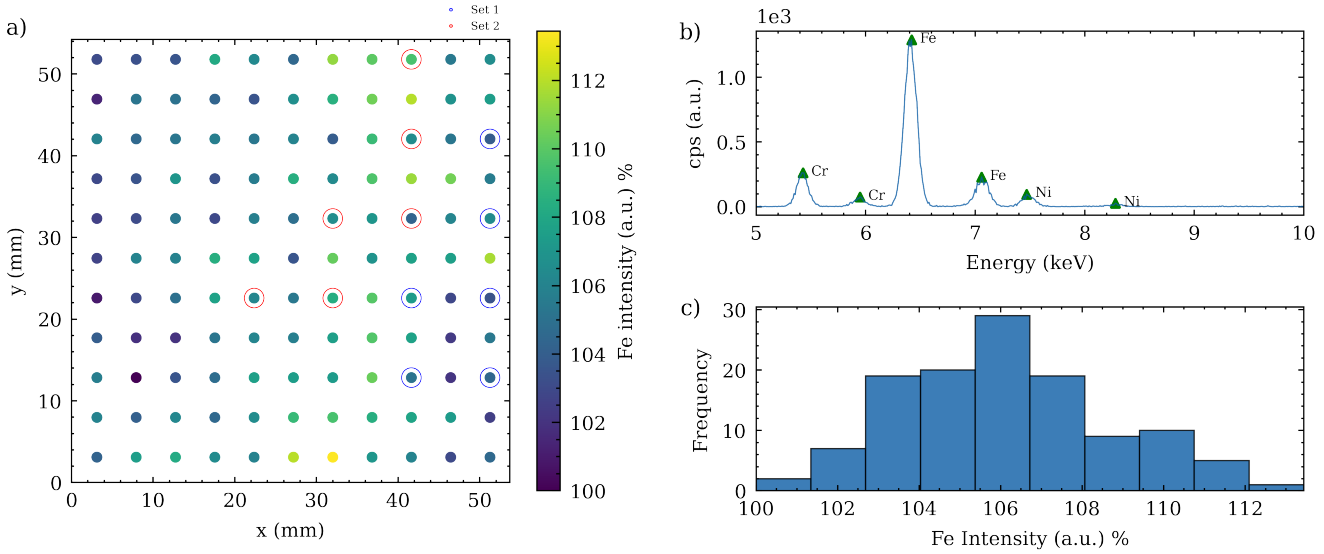

Figure 2. a) Spatial distribution of the integrated relative Fe signal intensity from screen printed electrodes, as measured by X-ray Fluorescence (XRF). The Fe signal is integrated over a circular area of 1.8 mm in diameter at each measurement point, with color coding indicating the intensity percentage. Set 1 and Set 2 refer to two different batches under which the electrodes were tested, showcasing potential variability in Fe distribution across the samples. b) Averaged XRF spectrum representing cumulative signals from one of the screen-printed spots, highlighting characteristic X-ray peaks. Peaks are labeled with corresponding elemental symbols, with prominent feature for Fe observed at around 6.4 keV. Other elements such as Cr and Ni are represented at their respective energies, illustrating the composition of the samples. c) Histogram representing the distribution of Fe intensity percentages across the measurement points. The distribution shows a rightward skew, with a predominant concentration of data points on the lower side of the Fe intensity scale. Despite the skew, the bulk of the data clusters around a central peak, suggesting an underlying normal distribution tendency with some deviations, possible due to variations in the screen-printing process or material heterogeneity.

contamination risks associated with electrolyte dispersion on the substrate. Additionally, this technique significantly reduces waste of active material. Unlike other coating methods such as doctor blading, which produce cut-out waste, screen-printing only coats the specific spots required for measurements.

The electrodes were coated as circular points with a 1.5 mm diameter, arranged in an $11x11$ square grid with each point spaced 4.9 mm apart. Details can be found in Section 3 of the supplementary materials. To evaluate the uniformity of the coating, these electrodes were analyzed using XRF. Figure 2a illustrates the distribution of Fe signal intensity across the grid, with the colorbar reflecting the relative Fe content as determined by the integrated signal at each point. As a direct measurement of the active material mass on this type of coating is challenging, the Fe signal in XRF images was used as a proxy for estimating Fe distribution and the active material content. By weighing the Al-foil before and after coating and drying, an average active material mass of 0.0218 mg was calculated. The Fe count per second (CPS) is centered around a central peak, indicating an underlying normal distribution with a maximum spread of $\pm 6.5\%$, as depicted in Figure 2c. Our two distinct sets of measurements are represented by red and blue markers in Figure 2a. The color distribution across the grid indicates a uniform Fe coating, although some areas exhibit higher or lower concentrations. This is crucial for evaluating the consistency of the screen-printing process. The XRF spectrum of a representative coated point is shown in Figure 2b and features Fe peaks at 6.41 keV and 7.06 keV. While the spectrum is primarily characterized by Fe, minor peaks for Cr and Ni indicate their subordinate presence. Additional elements including P and Al, with peaks at 2.02 keV and 20.19 keV respectively, are also identified. The peaks, with lower CPS, are detailed in Supp.3. In the electrochemical procedures, such as galvanostatic cycling, this data can be utilized for setting the correct current to achieve the desired C-rate during charging and discharging protocols. For CV, as employed in this study, the information is essential to normalize the obtained current response.

2.2.2 Reproducibility at electrochemical level

Electrochemical data that derived from the automated experiments orchestrated with Auto-MISCHBARES platform demonstrated high reliability, with no observable failures or hardware errors that could compromise the results. All the measurements are stored on-the-fly in our DMS. The CV profiles of LFP electrodes, cycled between 1.8 V and 4.7 V at a scan rate of 5 mV/s are presented for two identical experimental sets for comparison, as shown in Fig. 3a and Fig. 3b. The scan rate selected for our study was an order of magnitude higher than typically reported for battery electrodes[61]. This choice aimed to mitigate issues associated with electrolyte evaporation in our open setup. Such evaporation could disrupt electrical contact between the WE and the RE during measurement and increase salt concentrations in electrolyte[62]. However, these effects were minimized by using a fast scan rate and routine flushing of the SDC head with fresh electrolyte after each measurement. The high scan rate can cause the change of slope in current density for CV measurements[63].

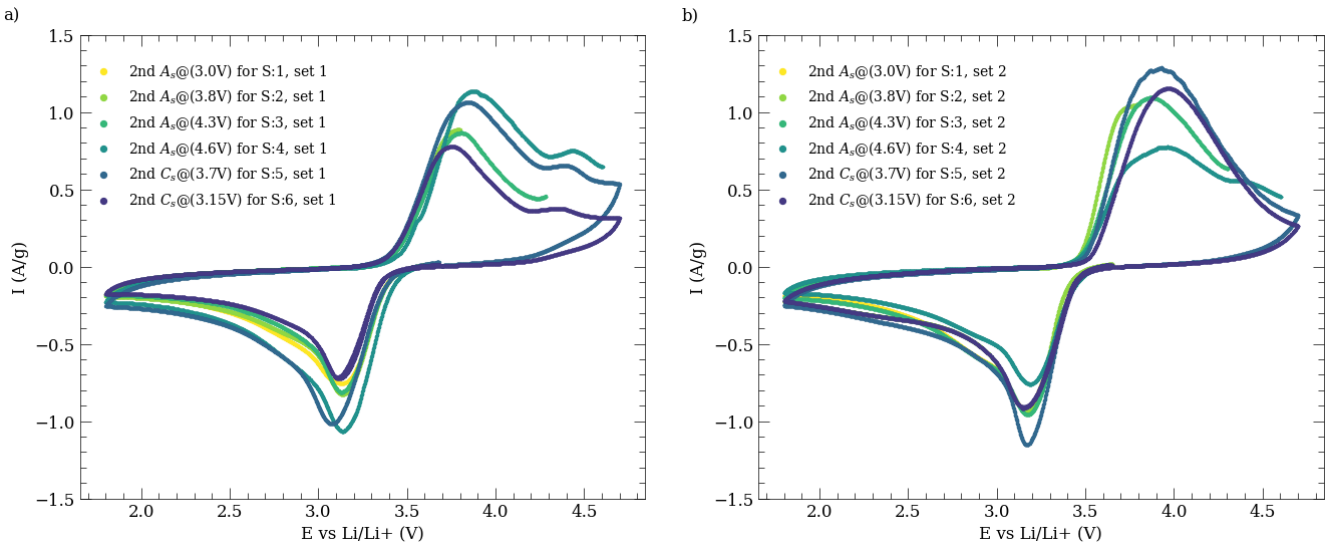

Figure 3. Demonstration of the second cycle of CV profiles derived from high-throughput experimentation utilizing Auto-MISCHBARES. Experiments were applied within a voltage range between 1.8 V and 4.7 V at a scan rate of 5 mV/s, starting from the open circuit potential (OPC) in the anodic direction. The CV curves reveal distinct redox peaks and the anodic peaks align closely at approximately 3.8 V while the corresponding cathodic peaks are positioned near 3.15 V, indicating similar consistent electrochemical response with a high degree of overlap across all measurements. a) illustrates the first set and b) the second, with each set consisting of six different experiments. For comparative analysis, CV tests that conclude at the same stop potential between the two batches, are color-matched. The exact termination potentials, corresponding to either the anodic or cathodic directions, are denoted in the legend.

In both sets of experiments, anodic and cathodic peaks were observed at approximately 3.8 V and 3.15 V, respectively, with a characteristic pair of redox peaks around 3.47 V corresponding to the charge-discharge reaction of Fe^{2+}/Fe^{3+}. In the first set, a minor anodic peak at 4.4 V was also detected, the origin of which remains unclear but aligns with findings reported by Chen et al.[64]. Our observed peak values, including anodic ones at 3.7 V, cathodic ones at 3.25 V, and half-wave potentials of 3.4 V at a scan rate of 0.1 mV/s, closely match those documented in their study. It is also important to mention that the reference potential was calibrated against a 5 mM ferrocene solution prior to experimentation.

In the first set of experiments, a slight shift in anodic peaks was observed, while the cathodic peak potential remained constant. The slight increased peak to peak separation, suggests lower reversibility[65,66], likely due to the higher scan rate[61,63] used in our measurements. However, the experiments were able to replicate features documented in related literatures[64,65]. The growing asymmetry in peaks, observed as measurements progressed, can be attributed to increasing conductivity constrains[64], a result of SEI growth at the CE and the RE, as these were not exchanged between measurements. In the second set of experiments, consistency was observed across all CV tests, with only minor variations in samples 4 and 5. The half-wave potential and peak separation showed a slight shift towards higher values. These changes in polarization might be partially attributed to the distance between the WE and the RE[67], or to an uneven substrate. Despite these complexities, the overall results from the SDC demonstrated a high degree of reproducibility across both sets of experiments. The synthesized CEI outcomes from these data are suitable for further exploration using ex-situ techniques.

2.2.3 Reproducibility at spectroscopic levels

Upon completing both sets of electrochemical experiments, the electrodes were rinsed with a PC solution, using SDC system to remove any residual dried electrolyte. After drying, an ex-situ XPS analysis was performed on the initial experimental set to evaluate the development of the CEI. This analysis identified various species and functional groups, as demonstrated in Figure. 4a across all panels, which presents the spectra from sample 1 (S1) of this set. The C=C peak, representative of the conductive carbon at the electrode surface, was selected as the reference with a relative concentration of 1. All subsequent signals are scaled and normalized to this benchmark.

Within the C1s region (Fig 4a, Panel I), a variety of carbon-containing species were identified. Peaks at 284.3 eV and 284.8 eV correspond to sp^2 (C=C) and sp^3 (C-C) carbon bounds, respectively. Additional peaks at higher binding energy, such as 286.3 eV, 288.8 eV, and 290.7 eV, were assigned to C−O, carboxyl (O−C=O), and carbonates CO_3 groups. In other samples of this set, a C=O signal was also detected near 287.8 eV (Supp.7 and Supp. 9). These signals are complemented by corresponding peaks in the O1s region, with a major contribution from C−O bonds, centered at 532.4 eV (Fig 4a, Panel II). In the F1s spectrum (Fig 4a, Panel IV), the residuals from the $LiPF_6$ salt is discernible at 688.0 eV. The remaining salt from the rinsing process suggests a need for further investigation by utilizing EMC or dimethyl carbonate (DMC) to potentially enhance the efficiency of the washing procedure, due to their higher $LiPF_6$ and lower LiF solubility. In the O1s region, fluorophosphates,

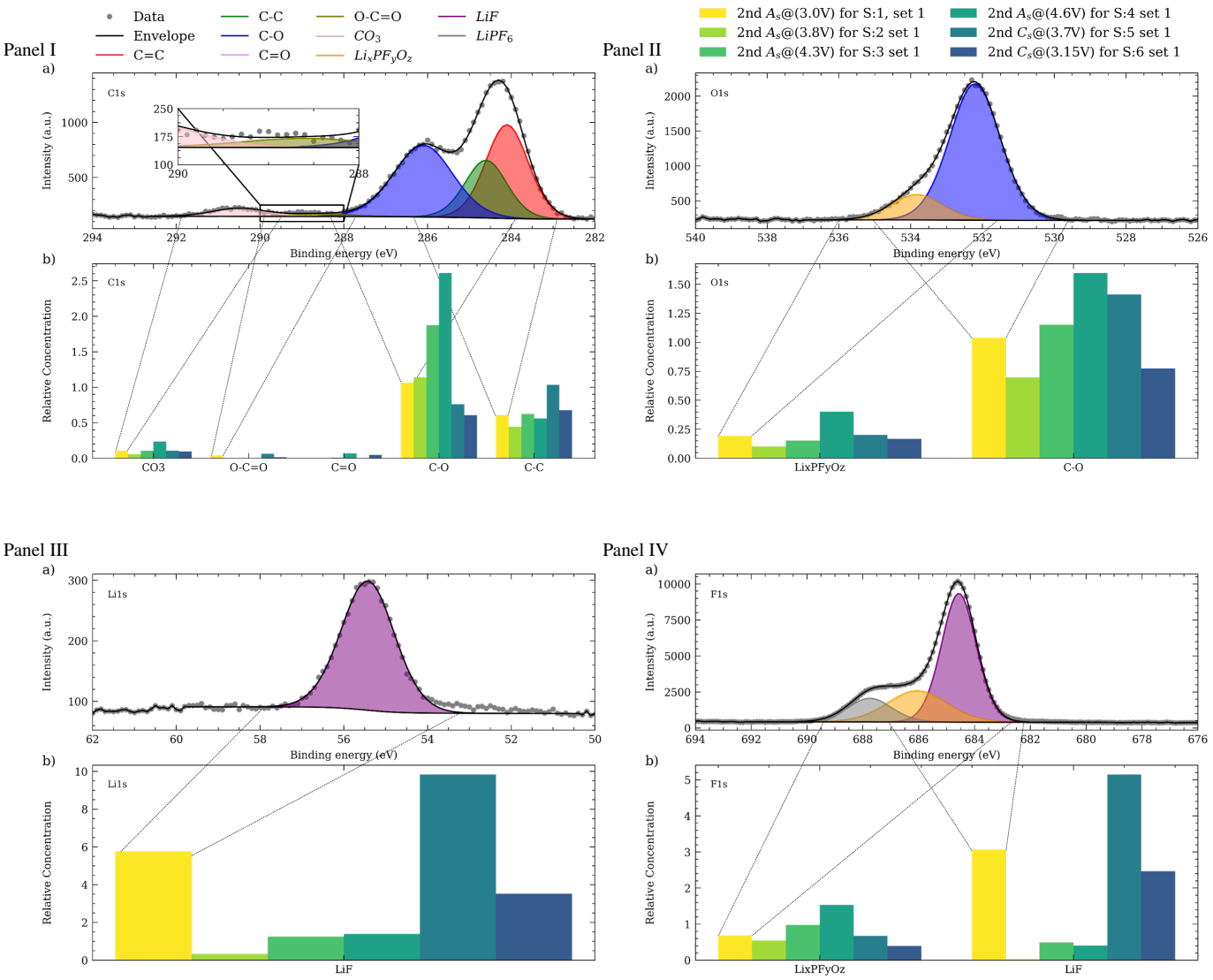

Figure 4. Characterization of the synthesized CEI from Auto-MISCHBARES on screen-printed electrode using ex-situ XPS analysis. In all Panels, a) present the XPS spectra of CEI from sample 1 (S1) in the first experimental series, obtained during the second anodic scan at the stopping potential of 3 V from the CV test. These spectra reveal the diverse chemical composition of this layer, with peaks corresponding to various functional groups and compounds: Panel I) C1s spectrum with multiple peaks indicative of carbon-based species, including C−C, C−O, and contributions from other carbon-oxygen groups. Panel II) The O1s spectrum with a peak for C−O bonds. Panel III) The Li1s region with presence of lithium-containing compounds depicted by LiF peak, originating from the decomposition of $LiPF_6$. Panel IV) The F1s region characterized by peaks associated with fluorinated compounds. Each chemical state identified is denoted by a distinct color in the spectra. The overlaid black line represents the envelope of the aggregated measured data, indicating the sum of contributions from all fitted peaks. The bottom bar charts b) provide a comparative analysis of the evolution of XPS signals for various species, observed from the first set and aligned by sequence of appearance in the CV tests, illustrating the binding energy signatures of specific chemical states within the CEI with relative concentration at these regions. The C=C peak intensity is set as a reference with the relative concentration of 1, representing the conductive carbon additive at the electrode surface, with other species normalized to this reference. The relative concentration of C−O in the C1s region shows a significant increase from sample 2 (S2) to sample 4 (S4), followed by a decrease in sample 5 (S5). In contrast, the LiF signal in the Li1s and F1s regions decreases up until S4 and then exhibits a sharp increase from S4 to S5. The behavior for $Li_xPF_yO_z$ species in the O1s and F1s regions follows a similar pattern to that of the C−O group.

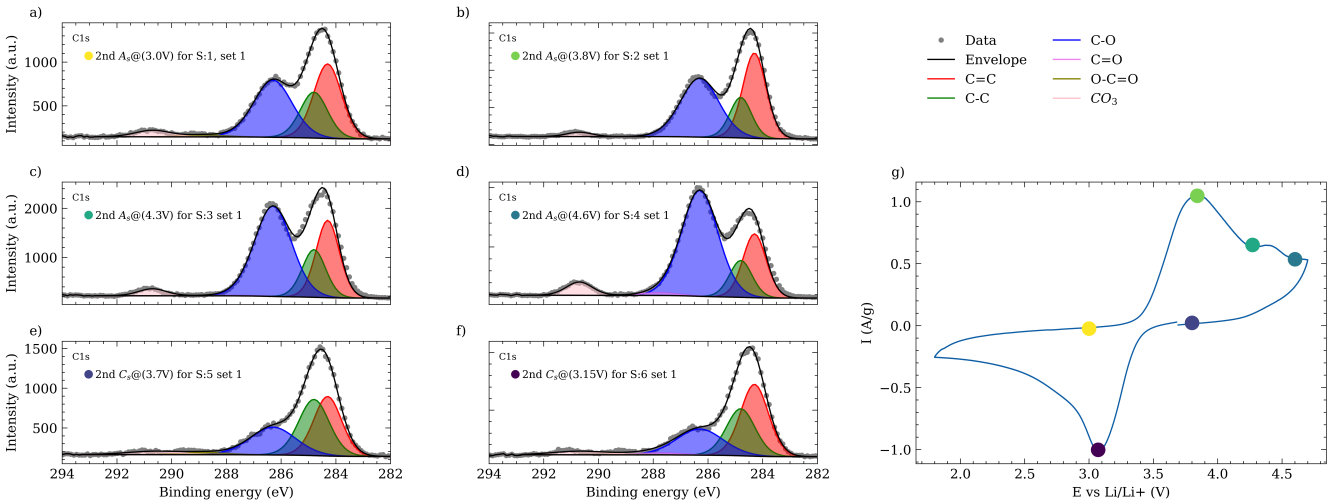

Figure 5. Representation of the XPS spectra in the C1s region for all samples from the first set of high-throughput experimentation (a-f). The key potentials at which measurements were paused during the second cycle of CV test are depicted in g. During the anodic scan (a-d), an increase in the intensity of signals from organic species, such as C−O, is observed, indicative of the evolving composition of the CEI. During the cathodic scan (e-f), this intensity decreases significantly.

as degradation products of $LiPF_6$ observed at 534.0 eV, with corresponding signals at 686.6 eV in the F1s region. The signal for LiF, indicating the presence of fluorinated and lithiated species, is evident at 684.8 eV in the F1s and 55.6 eV in the Li1s region (Fig 4a, Panel III). The similarity between the C−O and LixPFyOz compounds reflects the dynamic alterations of the CEI composition throughout the electrochemical cycling process.

Figure 4b for all panels, illustrate the evolution of the XPS signals across all the samples of this series. During the anodic scan of the CV measurement, an increase in the intensity of signals from organic species, such as C−O is observed in both C1s and O1s regions. These signals are attributed to the decomposition products of the electrolyte and contribute to the formation of the outer layer of the CEI. Notably, the increase in these signals becomes apparent in S3, at $4.3V$, coinciding with the peak of the anodic feature and subsequent potential elevation, consistent with findings reported by Kühn et al.[56]. In contrast, during the cathodic scan, the intensity of these species decreases significantly from 4.6 V to 3.7 V. This pattern further supported by Figure. 5, exhibiting the C1s trends across all samples. The observed increase in organic species during the anodic scan is indicative of a thickening of the CEI, presumably due to electrolyte decomposition at elevated voltages, which is supported by several studies[68–71] and evidenced by the reduced LiF signal from S1 to S4 (Fig. 4b, panel IV). During discharge, the cathodic scan shows an increasing LiF signal, suggesting the reformation of LiF, along with a decrease in C−O species[72]. At last, the XPS analysis validates the electrochemical data at every potential, pinpointing key regions within the CV profile. This correlation further enhances the integrity of our designed Auto-MISCHBARES workflow, contributing to the robustness and advancement of MAPs.

3 Conclusions

A critical question that arises with high-throughput platforms is whether they truly accelerate processes or inadvertently cause deceleration. Answering this, requires considering three key aspects: reliability, time efficiency, and reproducibility. Regarding reliability, Auto-MISCHBARES, represents a significant advancement in laboratory automation and scientific experimentation by integrating a comprehensive array of key components for robust, sequential experimentation. It covers a wide range of functionalities, from configuring and scheduling experiments to robust online control assessment, and provides real-time feedback on critical failures and experimental progress. Encompassing computer vision and statistical tools, the platform not only ensures the reliability of outcomes but also streamlines tasks to minimize researcher intervention and reduce human errors. Its real-time measurement capabilities, enable live visualization and can further optimize the workflow, from data acquisition to comprehensive analysis. The structured PostgreSQL database environment within the platform efficiently manages data formats, strengthen data correlation across multiple measurements and lays the ground for transfer learning. In our SDC system, the modifications to mechanical integrity are minimal as opposed to coin cell setups where disassembly can lead to the breaking of coatings at the edges of the electrodes, and sometimes even cause the coating to stick to the separator. Our SDC system is a more reliable and less intrusive approach to cell handling and is suitable for applications in electrochemical studies.

To establish time efficiency, our hierarchical framework demonstrates significant advantages due to its uninterrupted operational capabilities, which minimize the need for manual cell exchanges. For instance, considering our study scenario

where our substrate consists of 121 electrode spots, each requiring a one-hour CV test. In this case, our Auto-MISCHBARES platform, using the SDC head, would complete the measurements in 121 hours, with an additional 10 hours for rinsing, and moving for a total of 131 hours. On the contrary, the traditional manual approach would require extra time for cell assembly and disassembly, which takes an experienced researcher an additional 24 hours. Assuming an 8-hour workday without breaks, the manual process would span several days. Additionally, considering the limitation of processing only about 10 coin cells simultaneously due to channel availability in the cycler, this manual approach could extend the duration even further. While the measurement times are similar between our platform and manual methods, our framework's ability to operate continuously substantially enhances the time efficiency. As demonstrated in our previous study[31], the capability of our framework for parallelization across multiple SDCs as well as its integration with AL frameworks can further accelerate the process.

To address the final aspect of reproducibility, our platform proves validity in both electrode fabrication and electrochemical measurements. The use of screen-printing to create miniaturized, defined areas of measurements not only saves materials but also facilitates automated ex-situ analysis. This is attributed to the precisely arranged grid of measurement positions established by the screen-printed mask on the substrate. Further enhancements in future studies can be achieved by integrating XRF measurement results into the platform, allowing for the identification of mask defects and the selection of points with minimal deviation, thus reducing issues related to electrode thickness variation. Such variations can also effect the distance between the WE and RE, potentially leading to deviations in measurements[63]. These challenges can be further minimized by directly coating onto the substrate holder and avoid the use of a bendable foil for electrode fabrication. The consistency of our high-throughput electrochemical protocols, along with their correlation with XPS results that aligned with findings in the literature, further underscore the reproducibility and fidelity of our system. Auto-MISCHBARES enables in-depth investigation into the synthesis of SEI/CEI, especially for post-lithium battery materials, an area that still holds vast potential for exploration.

Integrating the comprehensive capabilities of our platform, we establish a trustworthy foundation with online analytical characterization, robust data fidelity and management systems. This integration facilitates the incorporation of ML and AL algorithms, enhancing decision-making and accelerating material optimization. Our hierarchical web server framework, which has been previously integrated with AL, now allows for further integration with more complex experimental planning algorithms such as Chimera[73] and Griffyn[74]. Additionally, for future study, the inclusion of cutting-edge approaches such as large language modeling (LLM) can further assist researchers[13], steering us towards the ultimate goal of a fully reliable material acceleration platforms. Our user-friendly framework, committed to digitalization and technological integration, represents a crucial step towards the development of fully autonomous laboratories, which can significantly expanding the scope of scientific exploration.

4 Code availability

Data, supporting the findings of this study, are available online at https://doi.org/10.5281/zenodo.10444324. The MISCHBARES framework[45] can be cloned from https://github.com/fuzhanrahmanian/MISCHBARES. In addition, videos recorded from our fully autonomous workflow[51] can be accessed at https://doi.org/10.5281/zenodo.10445749.

Acknowledgements

This work contributes to TUM.Battery, the Munich Data Science Institute, and the Munich Institute for Robotic and Machine Intelligence. This work contributes to the research performed at CELEST (Center for Electrochemical Energy Storage Ulm-Karlsruhe) and was partly funded by the German Research Foundation (DFG) under Project ID 390874152 (POLiS Cluster of Excellence). This project also received funding from the European Union's Horizon 2020 research and innovation program under grant agreement No 957189. The project is part of BATTERY 2030+, the large-scale European research initiative for inventing sustainable batteries for the future, funded by European Union's Horizon 2020 research and innovation program under Grant Agreement No. 957213 (BIG-MAP). HSS acknowledges funding from German Research Foundation (DFG) under Project ID 390776260 (eConversion Cluster of Excellence).

Author contributions statement

F.R conceived the experiments, design the data analysis MADAP and MISCHBARES software, developed the quality control protocols, validation tests and user interface. H.S.S prepared the mask for screen printing. S.F prepared the electrodes material and coated them onto the printed mask. F.R and S.F assisted in experimention and S.F characterized the samples by applying XPS. All authors reviewed the manuscript.

Additional information

Additional information can be found in the supplementary section.

References

1. Stein, H. S. Advancing data-driven chemistry by beating benchmarks. *Trends Chem.* **4**, 682–684, DOI: 10.1016/j.trechm.2022.05.003 (2022).
2. Stach, E. *et al.* Autonomous experimentation systems for materials development: A community perspective. *Matter* **4**, 2702–2726, DOI: 10.1016/j.matt.2021.06.036 (2021).
3. Roch, L. M. *et al.* Chemos: An orchestration software to democratize autonomous discovery. *PLoS One* **15**, e0229862, DOI: 10.1371/journal.pone.0229862 (2020).
4. Seifrid, M. *et al.* Autonomous chemical experiments: Challenges and perspectives on establishing a self-driving lab. *Accounts Chem. Res.* **55**, 2454–2466, DOI: 10.1021/acs.accounts.2c00220 (2022).
5. Gongora, A. E. *et al.* A bayesian experimental autonomous researcher for mechanical design. *Sci. advances* **6**, eaaz1708, DOI: 10.1126/sciadv.aaz1708 (2020).
6. Nikolaev, P. *et al.* Autonomy in materials research: a case study in carbon nanotube growth. *npj Comput. Mater.* **2**, 1–6, DOI: 10.1038/npjcompumats.2016.31 (2016).
7. Dave, A. *et al.* Autonomous optimization of non-aqueous li-ion battery electrolytes via robotic experimentation and machine learning coupling. *Nat. communications* **13**, 5454, DOI: 10.1038/s41467-022-32938-1 (2022).
8. Shi, Y., Prieto, P. L., Zepel, T., Grunert, S. & Hein, J. E. Automated experimentation powers data science in chemistry. *Accounts Chem. Res.* **54**, 546–555, DOI: 10.1021/acs.accounts.0c00736 (2021).
9. Abolhasani, M. & Kumacheva, E. The rise of self-driving labs in chemical and materials sciences. *Nat. Synth.* **2**, 483–492, DOI: 10.1038/s44160-022-00231-0 (2023).
10. Ament, S. *et al.* Autonomous materials synthesis via hierarchical active learning of nonequilibrium phase diagrams. *Sci. Adv.* **7**, eabg4930, DOI: 10.1126/sciadv.abg4930 (2021).
11. Ramprasad, R., Batra, R., Pilania, G., Mannodi-Kanakkithodi, A. & Kim, C. Machine learning in materials informatics: recent applications and prospects. *npj Comput. Mater.* **3**, 54, DOI: 10.1038/s41524-017-0056-5 (2017).
12. Vriza, A., Chan, H. & Xu, J. Self-driving laboratory for polymer electronics. *Chem. Mater.* **35**, 3046–3056, DOI: 10.1021/acs.chemmater.2c03593 (2023).
13. Zheng, Z., Zhang, O., Borgs, C., Chayes, J. T. & Yaghi, O. M. Chatgpt chemistry assistant for text mining and the prediction of mof synthesis. *J. Am. Chem. Soc.* **145**, 18048–18062, DOI: 10.1021/jacs.3c05819 (2023). PMID: 37548379.
14. Pendleton, I. M. *et al.* Experiment specification, capture and laboratory automation technology (escalate): a software pipeline for automated chemical experimentation and data management. *MRS Commun.* **9**, 846–859, DOI: 10.1557/mrc.2019.72 (2019).
15. Stein, H. S. *et al.* From materials discovery to system optimization by integrating combinatorial electrochemistry and data science. *Curr. Opin. Electrochem.* **35**, 101053, DOI: 10.1016/j.coelec.2022.101053 (2022).
16. Amici, J. *et al.* A roadmap for transforming research to invent the batteries of the future designed within the european large scale research initiative battery 2030+. *Adv. energy materials* **12**, 2102785, DOI: 10.1002/aenm.202102785 (2022).
17. Ling, C. A review of the recent progress in battery informatics. *npj Comput. Mater.* **8**, 33, DOI: 10.1038/s41524-022-00713-x (2022).
18. Su, L., Ferrandon, M., Kowalski, J. A., Vaughey, J. T. & Brushett, F. R. Electrolyte development for non-aqueous redox flow batteries using a high-throughput screening platform. *J. The Electrochem. Soc.* **161**, A1905, DOI: 10.1149/2.0811412jes (2014).
19. Matsuda, S., Nishioka, K. & Nakanishi, S. High-throughput combinatorial screening of multi-component electrolyte additives to improve the performance of li metal secondary batteries. *Sci. Reports* **9**, 6211, DOI: 10.1038/s41598-019-42766-x (2019).
20. Dave, A. *et al.* Autonomous discovery of battery electrolytes with robotic experimentation and machine learning. *Cell Reports Phys. Sci.* **1**, DOI: 10.1016/j.xcrp.2020.100264 (2020).
21. Martín-Yerga, D., Kang, M. & Unwin, P. R. Scanning electrochemical cell microscopy in a glovebox: structure-activity correlations in the early stages of solid-electrolyte interphase formation on graphite. *ChemElectroChem* **8**, 4240–4251, DOI: 10.1002/celc.202101161 (2021).

22. Dieckh"ofer, S., Schuhmann, W. & Ventosa, E. Accelerated electrochemical investigation of li plating efficiency as key parameter for li metal batteries utilizing a scanning droplet cell. *ChemElectroChem* **8**, 3143–3149, DOI: 10.1002/celc.202100733 (2021).

23. Sliozberg, K. *et al.* High-throughput screening of thin-film semiconductor material libraries i: System development and case study for tiwo. *ChemSusChem* **8**, 1270–1278, DOI: 10.1002/cssc.201402917 (2015).

24. Yada, C. *et al.* A high-throughput approach developing lithium-niobium-tantalum oxides as electrolyte/cathode interlayers for high-voltage all-solid-state lithium batteries. *J. The Electrochem. Soc.* **162**, A722, DOI: 10.1149/2.0661504jes (2015).

25. Rajagopal, D. *et al.* Data-driven virtual material analysis and synthesis for solid electrolyte interphases. *Adv. Energy Mater.* **13**, 2301985, DOI: 10.1002/aenm.202301985 (2023).

26. Baird, S. G. & Sparks, T. D. What is a minimal working example for a self-driving laboratory? *Matter* **5**, 4170–4178, DOI: 10.1016/j.matt.2022.11.007 (2022).

27. Pollice, R. *et al.* Data-driven strategies for accelerated materials design. *Accounts Chem. Res.* **54**, 849–860, DOI: 10.1021/acs.accounts.0c00785 (2021).

28. Castelli, I. E. *et al.* Data management plans: the importance of data management in the big-map project. *Batter. & Supercaps* **4**, 1803–1812, DOI: 10.1002/batt.202100117 (2021).

29. Vogler, M. *et al.* Brokering between tenants for an international materials acceleration platform. *Matter* **6**, 2647–2665, DOI: 10.1016/j.matt.2023.07.016 (2023).

30. Guevarra, D. *et al.* Orchestrating nimble experiments across interconnected labs. *Digit. Discov.* **2**, 1806–1812, DOI: 10.1039/D3DD00166K (2023).

31. Rahmanian, F. *et al.* Enabling modular autonomous feedback-loops in materials science through hierarchical experimental laboratory automation and orchestration. *Adv. Mater. Interfaces* **9**, 2101987, DOI: 10.1002/admi.202101987 (2022).

32. Raghavan, P. *et al.* Dataset design for building models of chemical reactivity. *ACS Cent. Sci.* **9**, 2196–2204, DOI: 10.1021/acscentsci.3c01163 (2023).

33. Krenn, M. *et al.* On scientific understanding with artificial intelligence. *Nat. Rev. Phys.* **4**, 1–9, DOI: 10.1038/s42254-022-00518-3 (2022).

34. Benayad, A. *et al.* High-throughput experimentation and computational freeway lanes for accelerated battery electrolyte and interface development research. *Adv. Energy Mater.* **12**, 2102678, DOI: 10.1002/aenm.202102678 (2022).

35. Rahmanian, F. *et al.* Attention towards chemistry agnostic and explainable battery lifetime prediction, DOI: 10.26434/chemrxiv-2023-nhdh2DOI:10.26434/chemrxiv-2023-nhdh2 (2023).

36. Pascazio, L. *et al.* Chemical species ontology for data integration and knowledge discovery. *J. Chem. Inf. Model.* **21**, 6569–6586, DOI: 10.1021/acs.jcim.3c00820 (2023).

37. Wilkinson, M. D. *et al.* The fair guiding principles for scientific data management and stewardship. *Sci. data* **3**, 1–9, DOI: 10.1038/sdata.2016.18 (2016).

38. Rohrbach, S. *et al.* Digitization and validation of a chemical synthesis literature database in the chempu. *Science* **377**, 172–180, DOI: 10.1126/science.abo0058 (2022).

39. Christensen, M. *et al.* Automation isn't automatic. *Chem. Sci.* **12**, 15473–15490, DOI: 10.1039/D1SC04588A (2021).

40. Shiri, P. *et al.* Automated solubility screening platform using computer vision. *Iscience* **24**, 102176, DOI: 10.1016/j.isci.2021.102176 (2021).

41. Eppel, S., Xu, H., Bismuth, M. & Aspuru-Guzik, A. Computer vision for recognition of materials and vessels in chemistry lab settings and the vector-labpics data set. *ACS central science* **6**, 1743–1752, DOI: 10.1021/acscentsci.0c00460 (2020).

42. Smith, G. & Dickinson, E. J. Error, reproducibility and uncertainty in experiments for electrochemical energy technologies. *nature communications* **13**, 6832, DOI: 10.1038/s41467-022-34594-x (2022).

43. Daboss, S., Rahmanian, F., Stein, H. S. & Kranz, C. The potential of scanning electrochemical probe microscopy and scanning droplet cells in battery research. *Electrochem. Sci. Adv.* **2**, e2100122, DOI: 10.1002/elsa.202100122 (2022).

44. Burger, B. *et al.* A mobile robotic chemist. *Nature* **583**, 237–241, DOI: 10.1038/s41586-020-2442-2 (2020).

45. Rahmanian, F. Auto-MISCHBARES, DOI: 10.5281/zenodo.10446337 (2023).

46. Bokeh Development Team. *Bokeh: Python library for interactive visualization* (2018).

47. Back, S. *et al.* Accelerated chemical science with ai. *Digit. Discov.* DOI: 10.1039/D3DD00213F (2024).

48. Maffettone, P. M. *et al.* What is missing in autonomous discovery: Open challenges for the community. *Digit. Discov.* **2**, 1644–1659, DOI: 10.1039/D3DD00143A (2023).

49. Grinberg, M. *Flask web development: developing web applications with python* (" O'Reilly Media, Inc.", 2018).

50. Bradski, G. The OpenCV Library. *Dr. Dobb's J. Softw. Tools* (2000).

51. Rahmanian, F. Auto-mischbares: Tutorial & demonstration, DOI: 10.5281/zenodo.10445749 (2023).

52. Rahmanian, F. Modular and Autonomous Data Analysis Platform (MADAP)", DOI: 10.5281/zenodo.10357192 (2023).

53. Draxl, C. & Scheffler, M. The nomad laboratory: from data sharing to artificial intelligence. *J. Physics: Mater.* **2**, 036001, DOI: 10.1088/2515-7639/ab13bb (2019).

54. Uhrin, M., Huber, S. P., Yu, J., Marzari, N. & Pizzi, G. Workflows in aiida: Engineering a high-throughput, event-based engine for robust and modular computational workflows. *Comput. Mater. Sci.* **187**, 110086, DOI: 10.1016/j.commatsci.2020.110086 (2021).

55. Medina, J. *et al.* Accelerating the adoption of research data management strategies. *Matter* **5**, 3614–3642, DOI: 10.1016/j.matt.2022.10.007 (2022).

56. Kühn, S. P., Edström, K., Winter, M. & Cekic-Laskovic, I. Face to face at the cathode electrolyte interphase: from interface features to interphase formation and dynamics. *Adv. Mater. Interfaces* **9**, 2102078, DOI: 10.1002/admi.202102078 (2022).

57. Wang, H. *et al.* Formation and modification of cathode electrolyte interphase: A mini review. *Electrochem. Commun.* **122**, 106870, DOI: 10.1016/j.elecom.2020.106870 (2021).

58. Chen, X., Shen, W., Vo, T. T., Cao, Z. & Kapoor, A. An overview of lithium-ion batteries for electric vehicles. In *2012 10th International Power & Energy Conference (IPEC)*, 230–235, DOI: 10.1109/ASSCC.2012.6523269 (IEEE, 2012).

59. Anseán González, D. *et al.* Evaluation of lifepo4 batteries for electric vehicle applications. In *Conference and Exhibition-2013 International Conference on New Concepts in Smart Cities: Fostering Public and Private Alliances, SmartMILE 2013*, DOI: 10.1109/SmartMILE.2013.6708211 (2013).

60. Ayuso, P., Beltran, H., Segarra-Tamarit, J. & Pérez, E. Optimized profitability of lfp and nmc li-ion batteries in residential pv applications. *Math. Comput. Simul.* **183**, 97–115, DOI: 10.1016/j.matcom.2020.02.011 (2021).

61. Mao, M. *et al.* In-situ construction of hierarchical cathode electrolyte interphase for high performance lini0. 8co0. 1mn0. 1o2/li metal battery. *Nano Energy* **78**, 105282, DOI: 10.1016/j.nanoen.2020.105282 (2020).

62. Pan, Y., Wang, G. & Lucht, B. L. Cycling performance and surface analysis of lithium bis (trifluoromethanesulfonyl) imide in propylene carbonate with graphite. *Electrochimica Acta* **217**, 269–273, DOI: 10.1016/j.electacta.2016.09.080 (2016).

63. Ming, J., Li, M., Kumar, P. & Li, L.-J. Multilayer approach for advanced hybrid lithium battery. *Acs Nano* **10**, 6037–6044, DOI: 10.1021/acsnano.6b01626 (2016).

64. Chen, Z.-Y., Zhu, H.-L., Wei, Z., Zhang, J.-L. & Li, Q.-F. Electrochemical performance of carbon nanotube-modified lifepo4 cathodes for li-ion batteries. *Transactions Nonferrous Met. Soc. China* **20**, 614–618, DOI: 10.1016/S1003-6326(09)60187-4 (2010).

65. Hou, J. *et al.* Lithium-gold reference electrode for potential stability during in situ electron microscopy studies of lithium-ion batteries. *J. The Electrochem. Soc.* **167**, 110515, DOI: 10.1149/1945-7111/ab9eea (2020).

66. Huynh, L. T. N. *et al.* Electrode composite lifepo 4@ carbon: Structure and electrochemical performances. *J. Nanomater.* **2019**, 2464920, DOI: https://doi.org/10.1155/2019/2464920 (2019).

67. Elgrishi, N. *et al.* A practical beginner's guide to cyclic voltammetry. *J. chemical education* **95**, 197–206 (2018).

68. Mahne, N., Renfrew, S. E., McCloskey, B. D. & Freunberger, S. A. Electrochemical oxidation of lithium carbonate generates singlet oxygen. *Angewandte Chemie Int. Ed.* **57**, 5529–5533, DOI: 10.1002/anie.201802277 (2018).

69. Wang, R. *et al.* Electrochemical decomposition of li2co3 in nio–li2co3 nanocomposite thin film and powder electrodes. *J. Power Sources* **218**, 113–118, DOI: 10.1016/j.jpowsour.2012.06.082 (2012).

70. Tasaki, K. *et al.* Solubility of lithium salts formed on the lithium-ion battery negative electrode surface in organic solvents. *J. The Electrochem. Soc.* **156**, A1019, DOI: 10.1149/1.3239850 (2009).

71. Yin, Z.-W. *et al.* Revealing of the activation pathway and cathode electrolyte interphase evolution of li-rich 0.5 li2mno3· 0.5 lini0. 3co0. 3mn0. 4o2 cathode by in situ electrochemical quartz crystal microbalance. *ACS applied materials & interfaces* **11**, 16214–16222, DOI: 10.1021/acsami.9b02236 (2019).

72. Li, Q. *et al.* Investigations on the fundamental process of cathode electrolyte interphase formation and evolution of high-voltage cathodes. *ACS applied materials & interfaces* **12**, 2319–2326, DOI: 10.1021/acsami.9b16727 (2019).

73. Häse, F., Roch, L. M. & Aspuru-Guzik, A. Chimera: enabling hierarchy based multi-objective optimization for self-driving laboratories. *Chem. science* **9**, 7642–7655, DOI: 10.1039/C8SC02239A (2018).

74. Häse, F., Aldeghi, M., Hickman, R. J., Roch, L. M. & Aspuru-Guzik, A. Gryffin: An algorithm for bayesian optimization of categorical variables informed by expert knowledge. *Appl. Phys. Rev.* **8**, 031406, DOI: 10.1063/5.0048164 (2021).